High cycle fatigue life estimation of AlSi10Mg processed by laser powder bed fusion

Even W. Hovig[1,*], *Amin* S. Azar[2], *Martin* F. Sunding[2], *Knut* Sørby[1], *Mohammed* M'hamdi[2] and *Erik* Andreassen[2]

[1]Norwegian University of Science and Technology, 7031 Trondheim, Norway
[2]SINTEF Industry, 0373 Oslo, Norway

Abstract. Fatigue life is known to be dependent on the surface properties of the material. Surface roughness provokes local stress concentration and cause crack initiation even at minute cyclic loads. In laser powder bed fusion, the as-built surfaces show variable roughness depending on the orientation of the specimens with respect to the build plate. In order to analyse the effect of build angle on surface properties, flat tensile specimens were produced from an AlSi10Mg alloy in a Concept Laser M2 Cusing machine. Seven specimens were arranged from flat to perpendicular with respect to the build plate at 15° intervals. The as-built surface topography of each specimen was characterised by white light interferometry. Two methods for calculating the stress concentration factor for high cycle fatigue simulation were developed. The presence of sub-surface porosity was a crucial factor in expanding the stress concentration as demonstrated by finite element analysis.

1 Introduction

Additive manufacturing (AM) is a process where material is added layer by layer to form a three-dimensional part. In laser metal powder bed fusion (LPBF) the feedstock material, typically in the form of a pre-alloyed powder, is distributed over a substrate before each layer is melted by a laser to form a solid bond with the previous layer. AlSi10Mg is an alloy typically used in casting of parts with complex geometry and thin walls. For the alloy to be used in demanding applications such as automotive and aerospace, detailed knowledge of the high-cycle fatigue life is of high importance. This study aims to give designers a guideline for estimating the fatigue life of LPBF AlSi10Mg components based on internal and superficial defects.

The fatigue life of AM components is affected by several phenomena; surface characteristics, internal porosity, sub-surface porosity, and microstructure. Surface treatments have been found to significantly increase the fatigue life of AlSi10Mg [1]. When estimating the fatigue life of a component with defects it is common to estimate a stress concentration factor (SCF), $k_t = \sigma_{max}/\sigma_{nom}$. The maximum stress observed is a function of the geometry of the defect. For a U-shaped surface defect, the SCF can be estimated

* Corresponding author: even.w.hovig@ntnu.no

according to equation (1), where d is the distance from the surface to the tip of the defect, and ρ is the radius at the tip [2].

$$K_t = 1 + 2\sqrt{\frac{d}{\rho}} \tag{1}$$

Depending on the cumulative stress concentration stemming from the type and size of defects in the component, either internal defects or surface defects will play a dominant role. Internal defects may be characterized either by non-destructive techniques such as X-ray computed tomography (CT) [3], or by destructive techniques such as microscopy of cross-sections.

Brandl et al. [4] conducted a systematic study where the effect of several parameters on high cycle fatigue life (R = 0.1) were investigated. Their parameters included platform temperature (30°C or 300°C), building orientation (0°, 45°, or 90°), and heat treatment (as-built or T6). The specimen surfaces were machined after LPBF and, therefore, the effect of build orientation was only reflected in the metallurgy and the crystallographic texture, rather than a surface finish effect. Furthermore, complementary micrography in the mentioned study showed that the microstructure became homogeneous with random texture after solution treatment. This phenomenon was also observed in Al alloys with rolling texture [5]. The latter implies that the build orientation may not influence the fatigue life if the specimens are solution treated.

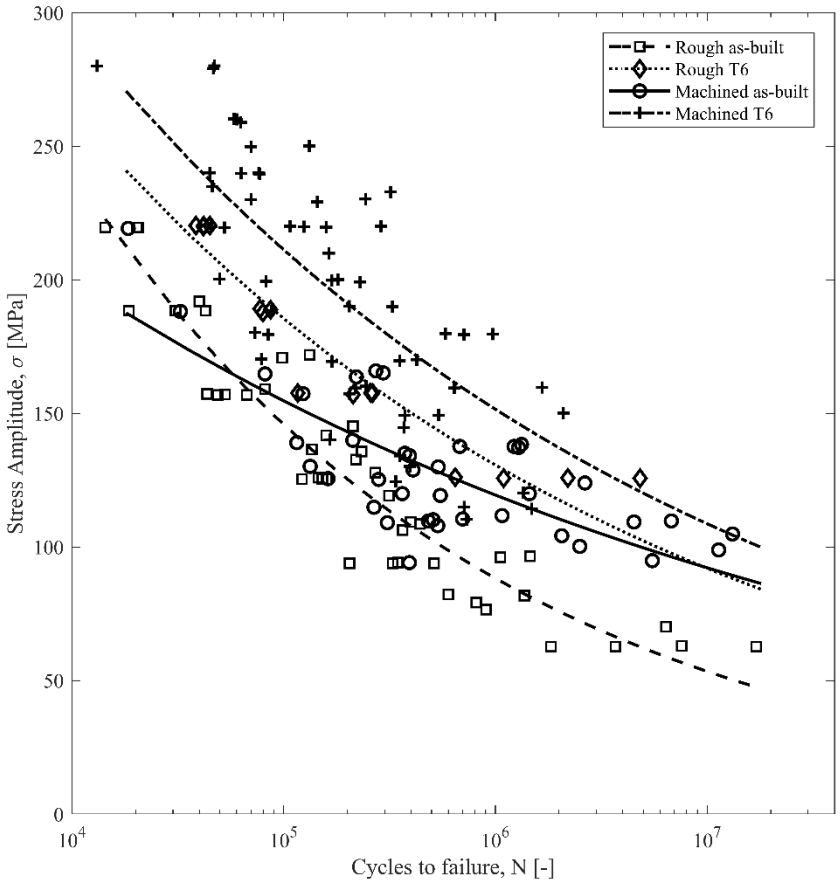

Figure 1 Compilation of fatigue life results from ref. [4, 6-8]. 'Rough' and 'Machined' refer to the surface condition, and 'as-built' and 'T6' refer to the heat treatment condition.

Maskerey et al. [6] investigated the effect of heat treatment on fatigue specimens (R = 0.1). They used specimens with as-built surface finish, all built parallel to the build direction. The results showed that solution treatment followed by T6 heat treatment reduced the tensile strength compared to the as-built (no heat treatment) and increased the fatigue resistance. Aboulkhair et al. [7] expanded the study by investigating differences between machined and as-built surfaces in addition to heat treatment. They showed that machining the surface did not increase the fatigue life at high stress levels, yet it increased the fatigue life at low stresses (high cycle fatigue).

Mower et al. [8] investigated the bending fatigue life (R = -1) of as-built and polished surfaces. In their work, the "as-built" surface finish was from specimens that were oriented at 0° and 90°, while the "polished" surface finish was from specimens that were oriented only at 0°. They also demonstrated that the tensile strength was higher for the 0° specimens, while no difference in fatigue strength was observed. Polishing the fatigue samples somewhat increased the fatigue life, but the presence of large voids that act as stress concentration sites reduces the effect of polishing.

Siddique et al. [3] developed a stochastic method for fatigue life prediction of AlSi12 processed by LPBF based on defect geometry, crack propagation tests, and fatigue tests. While accurate at high stress levels, at low stress levels the method failed to predict the fatigue life with acceptable precision.

Figure 1 compiles fatigue results from refs. [4, 6-8], highlighting the influence of surface condition and heat treatment. ‘Rough’ and ‘Machined’ refer to the surface condition, and ‘as-built’ and ‘T6’ refer to the heat treatment. Differences in laser processing parameters, platform temperature, and build orientation are neglected to highlight the low machine-to-machine repeatability. Fatigue test conditions are assumed to have minor effects. The figure shows that, starting with a specimen directly from the LPBF machine, heat treatment T6 has a larger effect on the fatigue life than machining the surface.

This study proposes two different methods for estimating the stress concentration factor of LPBF materials based on surface roughness measurements.

2 Materials and methods

As the initial step, a set of cubes were produced with different processing parameters to optimize the density of the material (c.f. density cube approach). The processing parameters that yields the highest density were selected for the subsequent specimens. The processing of samples was performed using Concept Laser M2 Cusing machine. The feedstock was supplied by GE Additive (CL31AL). The nominal chemical composition is listed in Table 1.

Table 1 Chemical composition of the powder from the supplier.

Si	Mg	Fe	Mn	Ti	Cu	Zn	C	Al
9.0-11.0	0.2-0.45	<0.55	<0.45	<0.15	<0.1	<0.1	<0.05	bal.

Flat dog bone specimens were produced with processing parameters according to Table 2. The island scan strategy was used, with island size of 5 mm×5 mm, X and Y shift of 1 mm, and angular shift of 45°. One additional contour scan was used, on the inside of the specimen surface perimeter. Each layer was first scanned with a low laser power of 50 W to bake and preheat the powder. Argon gas was used to shield the build chamber. Seven unique orientations were selected for surface topography characterization by white light interferometry (WLI). Table 3 shows the selected samples with annotation according to ISO/ASTM 52921:2013E.

Table 2 Laser parameters for the powder bed fusion.

Layer thickness, t	Hatch spacing, h	Laser power, P	Scan velocity, v
30 µm	97.5 µm	200 W	1200 mm/s

Table 3 Specimen annotation according to ISO/ASTM 52921:2013E

Specimen #	1	2	3	4	5	6	7
Designation	XY	XY+15B	XY+30B	XY+45B	XY+60B	XY+75B	ZX

The upward facing as-built surfaces was characterized by white light interferometry (Wyko NT-9800) and analysed in the Veeco Vision 4.2 software. Two areas of 1.7×2.3 mm were captured in the gauge region of each of the specimens. The raw data was filtered with a long wavelength pass Gaussian filter with spatial cut-off of 20 µm. Initial investigation revealed that partially melted powder particles were fused to the surface; therefore, the upper 'tail' of the distribution of the surface height was masked for the SCF estimation. Further analysis of the filtered topography was carried out with in-house scripts in Matlab.

3 Results and discussion

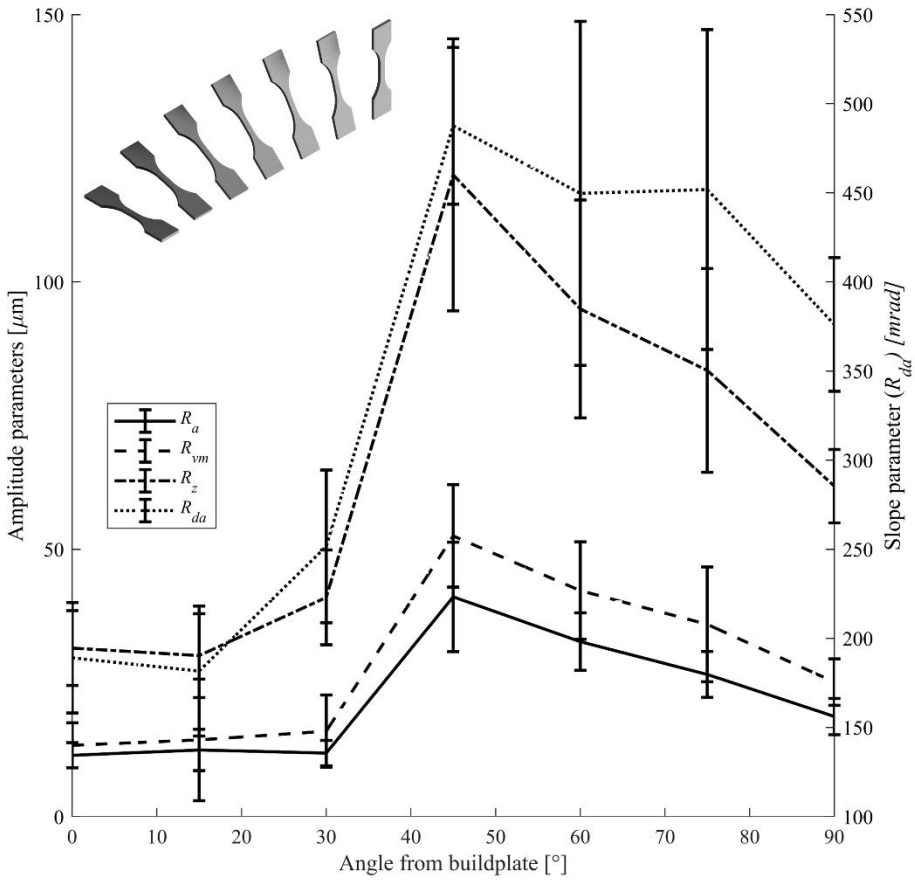

Figure 2 Selected roughness measurements for sample 1 through 7 (oriented from 0° to 90° with 15° increments). The inset shows the orientations of each specimen from 0° to 90 °.

Figure 2 shows selected surface roughness measurements for sample 1 through 7 over the area mapped with WLI. The arithmetical mean deviation of the roughness profile (R_a) is at the lowest for the samples oriented at 0°, 15°, and 30°, before a steep increase in surface roughness at 45°, followed by a decline in surface roughness as the samples are raised towards the 90° orientation. The average depth of the valleys (R_{vm}), the average distance between the peaks and the valleys (R_z), and the average absolute slope measured in radians (R_{da}) all follow the same trend as the arithmetical mean deviation (R_a).

The observed roughness is contradictory to LPBF roughness measurements reported by Boschetto et al. for AlSi10Mg [9], and by Strano et al. for stainless steel [10], in which the peak in roughness appeared at lower angles. As a result, the present surface roughness profile fits poorly with the model introduced by Boschetto et al. Several factors will determine the final surface roughness during specimen fabrication, such as powder particle size and morphology, and process parameters. As can be seen in the variation of the results from different studies (Figure 1), the machine-to-machine repeatability is low. Therefore, surface characterization for the specific process and material is necessary in order to predict the fatigue life of a LPBF component.

Figure 3(a) shows a polished cross-section of a cube with the process parameters and powder used in this study. The porosity content is measured to 0.50% and the distribution, pore diameter, and circularity of the pores as a function of distance from the edge are shown in Figure 3 (b). As can be seen in Figure 3 (a), there is a substantial amount of sub-surface porosity, and the closest distance between the surface and a pore is less than 15 µm. The measured diameter of the pores ranges from 8 µm to 175 µm, and the average diameter is 27 µm. The average circularity is 0.88, which indicates that the pores are dominantly spherical.

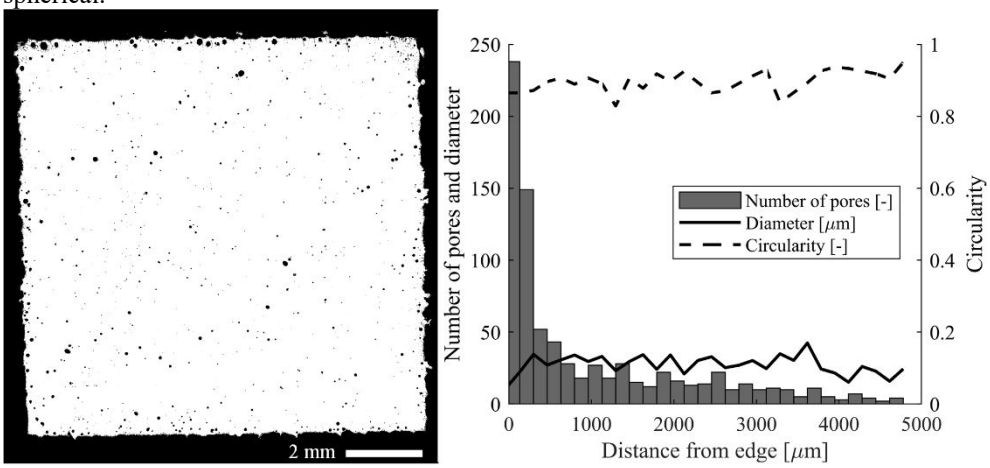

Figure 3 Optical microscopy image of a cross section of the material (left), and morphology analysis of the porosity (right).

In addition to introducing local stress concentrations, the superficial and internal defects affect each other. Figure 4 shows a numerically computed SCF, $k_t = \sigma_{max}/\sigma_{nom}$, for a generic material with a U-shaped groove on the surface and a spherical pore in close proximity to the crack tip under tensile load. As can be seen, both the pore diameter and the distance from the groove tip affect the local stress at the groove tip. The SCF increases for larger pores close to the groove tip, while it decreases if the pore diameter is reduced or the pore is moved further away from the groove tip. Siddique et al. [11] expressed the SCF of a pore as a function of the pore diameter and distance from the surface (no surface roughness), with values for k_t ranging from 1 to 1.178. When comparing the magnitude of the stress concentration from only surface defects (Eq. 1 and baseline in Fig. 4) and internal

pores (Siddique et al.) it becomes clear that SCFs from surface defects are far larger than those from only spherical pores.

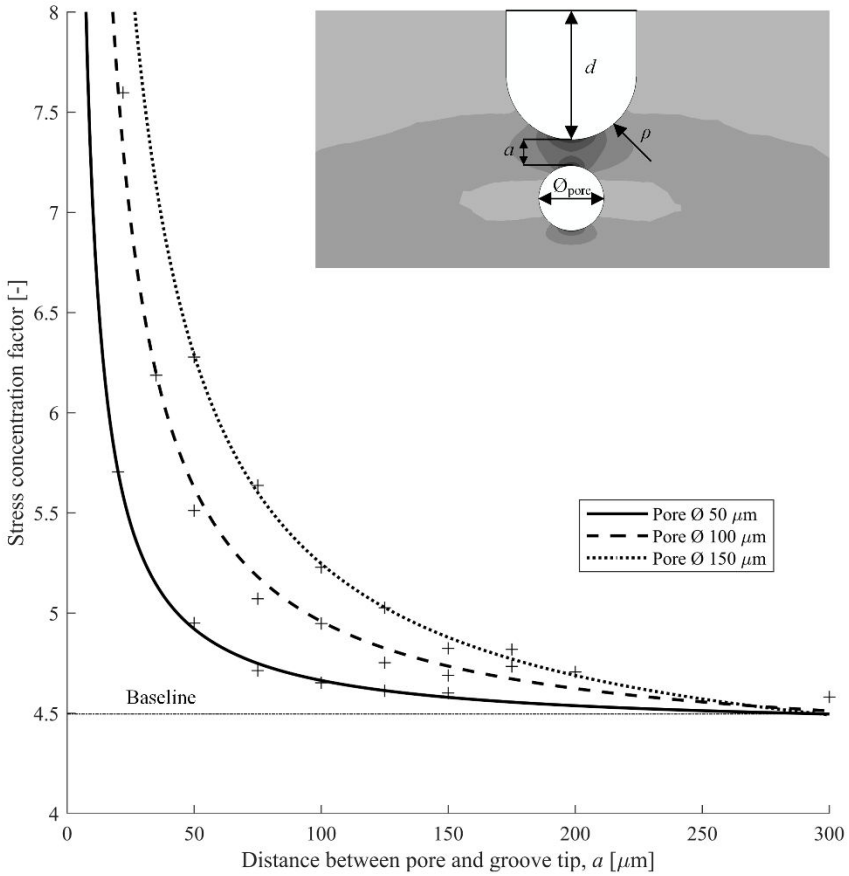

Figure 4 The effect of pore diameter and distance between pore and crack tip on the SCF of a U-shaped surface defect with nominal SCF of 4.5. The inset shows the relative geometry of the groove and the pore.

Consider the simplified schematic of a LPBF process inset in Figure 5. The figure shows a cross-section of three layers, where the scanning direction alternates with each layer. Each semi-circle represents a single laser track. The hatch spacing is indicated with h, the layer thickness with t, and the angle the surface is built at with respect to the horizontal build plate is indicated with θ. The surface can then be considered as a periodic row of laser tracks, where the depth of each valley (between two tracks) is the surface roughness measure R_v. The radius at the depth of the valley, ρ, can be calculated with equation (2);

$$\rho = \frac{L - tan(R_{da})\, R_z}{1 - tan(R_{da})} \tag{2}$$

where L is the width of the top of the valley, and R_{da} is the average angle of the slope of the valleys of the surface. The width L is the peak-to-peak distance measured as S (mean spacing between adjacent local peaks). The value of R_{da}, R_z, and S may be determined by WLI as shown in Figure 2, or simply with a perthometer. The SCF for surface defects may

then be calculated with equation (1) using R_v as d, and ρ according to equation (2). This method is referred to as the 'stylus method' in subsequent discussion.

An alternative approach for calculating the SCF of surface defects is to use the mapped topography from WLI. The surface topography is represented in a matrix, with each element, Z_{XY}, corresponding to the height of the pixel indicated by the row (X) and column (Y). The horizontal radius of curvature at each point may then be obtained based on a quadratic fit through that point and the adjacent points. If the data is fit to $Y = aZ^2 + bZ + c$, the spherical radius of curvature at X is approximately $r \cong (2a)^{-1}$. The SCF K_t may then be estimated using equation (1). This method is referred to as the 'WLI method' in subsequent discussion.

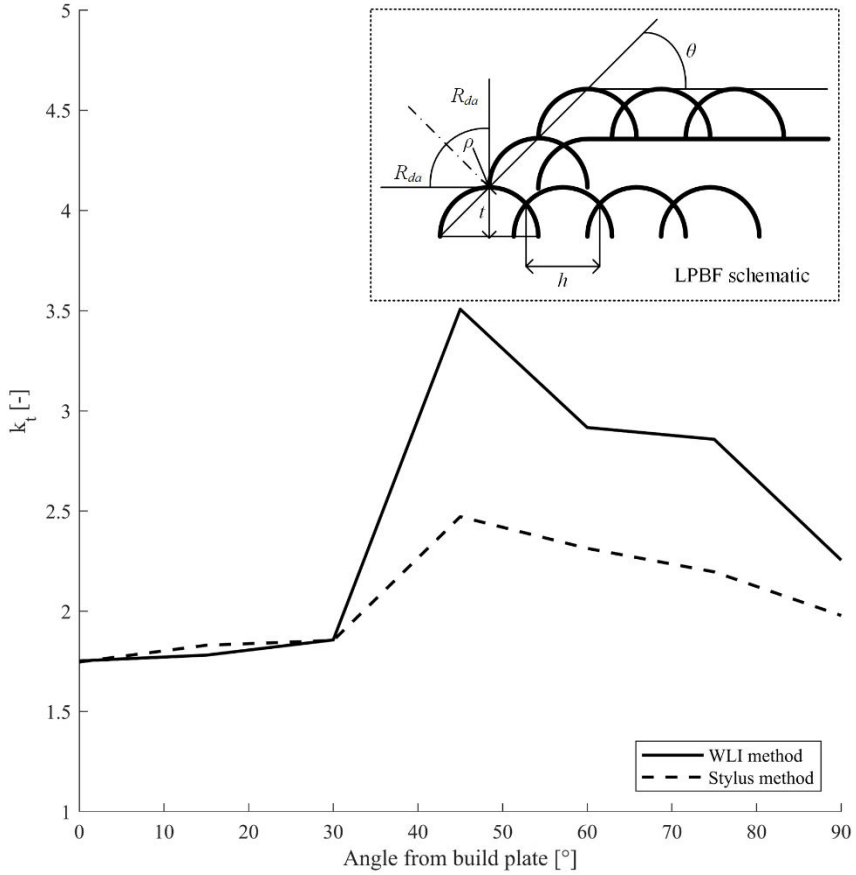

Figure 5 Estimated SCF for surface defects, k_t, for all specimen orientations with both the 'WLI method' and the 'stylus method'. Inset is a schematic of three layers of a LPBF process with the relevant parameters for the 'stylus method' indicated.

The estimated SCF for surface defects for the seven specimen orientations calculated using both the WLI method and the stylus method, are shown in Figure 5. As expected, the SCF follows the general trend of the surface roughness (Figure 2). For specimens oriented at angles below 45° the SCF is relatively low and consistent for both methods. When the surface roughness increases for the specimens oriented at 45° and above the WLI method is more conservative. The stylus method considers either a line on the surface (perthometer), or the average surface roughness in the investigated area (WLI). In both cases, the extremities of the peaks and valleys are given less weight, resulting in a less conservative estimate of the SCF. For smoother surfaces (0°, 15°, and 30°) the error is relatively small,

and the estimated SCF is acceptably conservative for the stylus method. If the surface is relatively rough, the WLI method will be a safer choice since it estimates a more conservative SCF.

If the material in question contains sub-surface pores, a modification of the estimated SCFs is needed. As shown in Figure 4 both pore diameter and the distance between the surface defect and the pore will increase the SCF of the surface defect. If a pore is in close proximity to the surface defect, dictated by some critical distance *a*, which is a function of the pore diameter, the SCF of the surface defect increases and will lead to premature crack initiation. However, as this crack propagates into the pore, the pore will blunt the crack. The effective SCF is then the SCF of the pore. Since the SCFs of pores are in the range of 1 to 1.178 [11], further crack propagation will be slowed down. Although sub-surface porosity might be present, it is unlikely it will be regularly distributed below the surface to blunt all cracks propagating. As a result, the SCF of the surface defects should be considered when designing components subjected to high cycle fatigue.

4 Conclusions

This study presents two methods for estimating stress concentration factors for high cycle fatigue life prediction of AlSi10Mg processed by laser powder bed fusion (LPBF). The stylus method gives a comparable estimate for smoother surfaces, but overestimates the fatigue life of rough surfaces when compared with the white light interferometry (WLI) method. The WLI method gives a more conservative estimate of the fatigue life for rougher surfaces.

In porosity free materials, the stress concentration factor, and thus the high cycle fatigue life, of LPBF AlSi10Mg is a function of the surface roughness.

The stress concentration factor of a surface defect is affected by internal pores, if the diameter of the pore is sufficiently large, and the distance between the surface defect and the pore is sufficiently small. Although the maximum stress at the surface defect increases, and promotes premature failure, the crack will be blunted when it propagates into the pore. Thus, the stress concentration factor of the surface defect should drive the fatigue life design.

The authors acknowledge funding from the Research Council of Norway (grant no. 248243, the MKRAM project) and SINTEF's strategic project on additive manufacturing, SIP-LAMINA.

References

1. S. Bagherifard, N. Beretta, S. Monti, M. Riccio, M. Bandini and M. Guagliano, Mater. Des., **145,** 28, (2018)
2. W. D. Pilkey and D. F. Pilkey; Peterson's stress concentration factors, (2008)
3. S. Siddique, M. Awd, J. Tenkamp and F. Walther, Eng Fail Anal, **79,** 34, (2017)
4. E. Brandl, U. Heckenberger, V. Holzinger and D. Buchbinder, Mater. Des., **34,** 159, (2012)
5. O. Engler and J. Hirsch, MSEA, **336,** 249, (2002)
6. I. Maskery, N. Aboulkhair, C. Tuck, R. Wildman, I. Ashcroft, N. Everitt and R. Hague, 26th Annual International Solid Freeform Fabrication Symposium, 1017,(2015)
7. N. T. Aboulkhair, I. Maskery, C. Tuck, I. Ashcroft and N. M. Everitt, Mater. Des., **104,** 174, (2016)
8. T. M. Mower and M. J. Long, MSEA, **651,** 198, (2016)
9. A. Boschetto, L. Bottini and F. Veniali, JMPT, **241,** 154, (2017)
10. G. Strano, L. Hao, R. M. Everson and K. E. Evans, JMPT, **213,** 589, (2013)

11. S. Siddique, M. Imran, M. Rauer, M. Kaloudis, E. Wycisk, C. Emmelmann and F. Walther, Mater. Des., **83,** 661, (2015)